ABSTRACT

NICHOLS, MIKAYLA BRIDGES. Torque Cancelling Equilibrium Operating Points of a Tethered Coaxial Dual-Rotor Ocean Current Turbine. (Under the direction of Dr. Matthew Bryant).

Hydrokinetic turbines are gaining popularity due to their ability to extract energy from ocean currents around the world. Due to the extreme seafloor depths where many of the most energetic currents are found, a tethered turbine is more economical than a rigidly mounted system. A counter-rotating coaxial turbine has two sets of rotors located along a common axis of rotation, with the upstream rotor producing torque and rotation in one direction while the downstream rotor produces torque and rotation in the opposite direction. If the upstream and downstream rotors' torques are unequal in magnitude, a net torque will exist which must be counteracted by the tether, which may lead to tether twisting and entanglement. While other methods can be utilized to counteract this torque imbalance, they require increasing the overall volume, cost, and mass of the system. To achieve passive torque cancellation between the upstream and downstream rotors in a single-tether system, the proposed system fixes the upstream blades to a generator's rotor and the downstream blades are fixed to the same generator's stator. Since there must be an equal and opposite reaction between the generator's stator and rotor, this achieves passive cancellation of torque. A method derived from Blade Element Momentum Theory is developed to find the upstream and downstream rotational speeds that yield equal magnitude, but opposite direction torques given a specified resistive load across the generator's terminals. This resistive load can be used to select the operating point of the system for a variety of fluid velocities for a fixed turbine geometry. The theoretical predictions of these equilibrium loci correlate well with experimental results. As the load resistance decreases, the magnitude of the torque cancelled increases while the rotational speed of both the upstream and downstream rotors remains approximately constant. A

linear relationship between all equilibrium loci and fluid velocities is observed, and the lower values of load resistance yield a higher coefficient of power for a fixed geometry. The mirroring of these trends in the predictions and experiments allow the model to be utilized to determine the optimal resistive load to accomplish the maximum energy extraction for a variety of flow speeds, where the geometry remains unchanged and there is no active control.

Torque Cancelling Equilibrium Operating Points of a Tethered Coaxial Dual-Rotor Ocean Current Turbine

by
Mikayla Bridges Nichols

A thesis submitted to the Graduate Faculty of
North Carolina State University
in partial fulfillment of the
requirements for the degree of
Master of Science

Mechanical Engineering

Raleigh, North Carolina

2021

APPROVED BY:

_____	_____
Dr. Matthew Bryant Committee Chair	Dr. Andre Mazzoleni
_____	
Dr. Kenneth Granlund	

BIOGRAPHY

Mikayla Bridges Nichols received her bachelor's degree in mechanical engineering with a minor in mathematical science from Clemson University, Clemson, SC, USA in 2019. Her research interests are primarily in dynamics and control.

ACKNOWLEDGMENTS

I gratefully acknowledge the Coastal Studies Institute and their North Carolina Renewable Ocean Energy Program for their funding of the coaxial hydrokinetic turbine. The tow system was supported by the U.S. Department of Energy under the award "Device Design and Robust Periodic Motion Control of an Ocean Kite System for Hydrokinetic Energy Harvesting (Award No. DE-EE0008635).

I would like to thank my advisor, Dr. Matthew Bryant, for his constant patience, guidance, and encouragement. He taught me to be a better engineer and pushed me to accomplish more than I thought I could.

I would like to thank my committee, Dr. Kenneth Granlund and Dr. Andre Mazzoleni, for their guidance and suggestions throughout my graduate career. Their impressive technical knowledge helped shape my studies, keep me on track, and troubleshoot any issues I ran into.

I would also like to thank all the students in the iSSRL lab for their encouragement, multiple reviews of this work, and their overall positive influence. Thank you to all, I could not have done it without you.

TABLE OF CONTENTS

LIST OF TABLES

LIST OF FIGURES

NOMENCLATURE

A	Cross-sectional area to flow [m^2]	τ_1	Nonequilibrium torque of upstream rotor [N·m]
C_P	Coefficient of power	τ_2	Nonequilibrium torque of downstream rotor [N·m]
C_{P1}	Coefficient of power of upstream rotor	τ_r	Nonequilibrium reaction torque between turbine and tether [N·m]
e_1	Induction factor of upstream rotor	$\tau_{holding}$	Holding torque of stepper motor [N·m]
e_2	Induction factor of downstream rotor	V_{RMS}	Root mean square voltage seen during experiment [V]
i	Current [A]	V_{Peak}	Peak voltage seen during motor constant experiment [V]
i_{rated}	Rated current of stepper motor [A]	v_∞	Fluid velocity [m/s]
K_e	Back emf constant [V·s/rad]	ω_1	Upstream rotational speed [rad/s]
K_τ	Torque constant [N·m/A]	ω_2	Downstream rotational speed [rad/s]
P	Power extracted [W]		
ρ	Density of fluid [kg/m^3]		
R_{load}	Load resistance [Ω]		
R_{arm}	Armature resistance [Ω]		
τ	Torque when in equilibrium [N·m]		

1. Introduction

Renewable energy has been a popular field of study in recent years as the world is moving away from its reliance on fossil fuels. One of the up-and-coming disciplines is that of marine hydrokinetic energy, which is produced by capturing the energy of moving water. Rather than damming water to use gravity to move the fluid rapidly over turbines, extracting energy from naturally flowing water is preferred for ecological and economic considerations [1]. One notable source of natural kinetic energy is the Gulf Stream, located near the shoreline of the eastern United States, which is convenient since the cost of energy increases quadratically with distance from port [2]. The highest fluid velocities, which provide the greatest amount of energy for extraction, are located near the surface, while the depth of the seafloor can be around 3000 m [3]. Although there are many configurations for implementing turbines in shallow waters with rigid mounts [4, 5, 6, 7], creating a fixed structure that reaches the surface from these depths would be impractical and costly to a point where the energy would no longer be economical to extract [8]. Hence, a flexible tether is the preferred design method compared to an inflexible support structure due to decreased costs. Turbines are the most common method of energy extraction and the easiest to install, so they will be examined in this paper. However, when using the tether configuration with one or more turbines, the torque that must be reacted to support the turbine(s) must be considered. If there is only one set of turbine blades, this will yield an imbalance of torque that will be transmitted to the tether, leading to tether twisting and likely entanglement. For this reason, a single-turbine, single-tether system with no additional control as depicted in **Fig. 1(a)** is generally infeasible. There are several methods to address this inherent torque imbalance: multiple tethers can be used to react the turbine torque via appropriately placed tension forces [9], the centers of buoyancy and gravity

can be appropriately spaced to create a restoring buoyancy moment [10], lifting control surfaces can be utilized to hydrodynamically react the torque and actively control orientation [11], and a bridle can be employed to create an additional moment arm for the tether tension force. However, each of these approaches add additional material, complexity, points of failure, and cost to the system. A passive solution to this problem is to have pairs of turbine rotor blades such that the torques generated are equal in magnitude but opposite in direction, resulting in zero net torque [12]. Rotor pairs can be configured by positioning them on parallel axes of rotation [12] or by having them coaxially located [13, 14] as demonstrated in **Figure 1(b)** and **Figure 1(c)**, respectively.

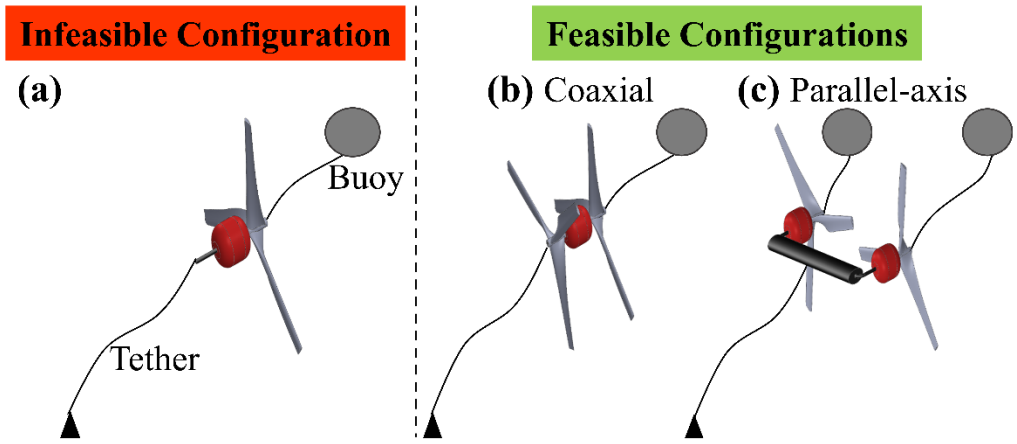

Figure 1. (a) Unbalanced torque from a single-rotor turbine can lead to tether twist and entanglement. Pairs of rotors can be arranged in either (b) coaxial or (c) parallel-axis configurations to produce zero net torque.

The parallel-axis configuration utilizes a central fairing structural member that, with counter-rotating rotors, experiences a 3-point bending loading scenario that requires significant structural reinforcement. Each rotor is exposed to similar flow regimes when on parallel axes, making passive torque cancellation achievable. Coaxial configurations can accomplish torque cancellation

by using separate generators for upstream and downstream rotors with an active torque control system, using a differential gearbox to combine the upstream and downstream shafts to a single generator input, or fixing one set of rotor blades to the rotor of a generator and the other set of rotor blades to the stator of the generator [13]. This last configuration, which is known as a direct drive counter-rotating generator, leads to passive torque cancellation as well as a significant decrease in structural mass when compared to the parallel-axis configuration. Another benefit of this configuration is that the counter-rotation of generator stator and rotor will increase the relative speed, with the potential to nearly double power output when compared to a stationary generator stator [15]. This configuration has been implemented for wind turbines on rigid mounts [16, 17, 18, 19] as well as for ocean turbines that are rigidly mounted [20] and on tethered configurations [21]. In the previous analytical and experimental hydrokinetic coaxial turbine studies, the downstream rotors are placed directly behind the upstream rotors. However, for a skewed turbine, a larger distance between the rotors of half rotor diameter can lead to an increase in power extraction due to fresh inflow to the downstream rotor [22, 23]. The increase in power under skew was examined experimentally on a rigid sting [24], but the modeling and testing of a tethered system with this rotor spacing and utilizing a direct drive counter-rotating generator has yet to be reported.

In this paper, the modeling and experimental analysis of a coaxial, hydrokinetic turbine with a direct drive counter-rotating generator are presented. The theoretical scope focuses on equilibrium loci generated by the rotor pair, including the upstream and downstream rotor speeds as well as the magnitude of the generated torque. An experimental campaign is completed to verify these trends. First, the mechanism by which a counter-rotating direct drive generator achieves passive torque cancellation is explained, followed by the derivation of these equilibrium loci and

an overview of the physical system that is used to validate the stability and operating point trends as design parameters are changed. The results of these theoretical and experimental campaigns are presented and then compared to one another. Once the comparison of theoretical and experimental results demonstrating the same trends is achieved, the model is used to predict optimal design parameters for maximum energy extraction.

2. Methodology

2.1. Passive torque cancellation from electromechanical coupling

The power extracted from a flow can be calculated as [25]:

$$P = \frac{1}{2} C_P \rho A v_\infty^3 \quad (1)$$

where P is power, C_P is the coefficient of power or the ratio of power extracted to power available within the flow, ρ is the density of the flow, A is the cross-sectional area, and v_∞ is the freestream fluid velocity. From Eq. (1), power increases cubically with v_∞. When the upstream rotor extracts energy from the flow, the velocity of the flow is decreased directly behind the upstream rotor. This reduces the inflow velocity to the downstream rotor, yielding lower dynamic pressure and available flow power at the downstream rotor with all else held constant. Knowing this, without any additional control or design considerations, the values of torque generated by the upstream and downstream rotors are not equal.

To make this energy harvesting device economically feasible, a mechanically simple and passive torque cancellation system that avoids tether entanglement due to the reaction torque with the tether, τ_t, is more economical than an active control system. Active control systems increase

costs for the design of the system, increase the number of failure points, and can increase weight of the system. The use of the generator as an electromechanical coupling of the upstream and downstream blades can provide this passive torque cancelation. In a typical generator arrangement operating in steady state, the mechanical torque input to the generator through the shaft generates an equal and opposite torque from the back electromotive force (back-emf) of the generator. This reaction takes place between the rotating rotor to which the mechanical torque was applied, and the stationary stator. In the case of a hydrokinetic turbine, this mechanical torque input will be from the hydrodynamic forces acting on the upstream blades, inducing τ_1. In this coaxial hydrokinetic turbine, instead of the stator being fixed to a stationary housing, it is fixed to the downstream blades of the turbine rotating in the opposite direction with a hydrodynamic torque, τ_2, acting upon it At steady state conditions, this arrangement enforces that the upstream blades, the rotor on stator, the stator on rotor, and the downstream blades all generate equal magnitude torques due to this requirement of equal and opposite steady-state electromagnetic torques within the generator. Hydrodynamically, this torque-cancelling equilibrium operation requires that the upstream and downstream blades assume differing rotation rates such that they experience equal magnitude, but opposite direction, fluid torques in their respective local flow speed environments. With equal magnitudes in opposite directions, this leads to a zero-reaction torque with the tether. A simplified free body diagram during steady state operating conditions is used to display this passive torque cancellation and can be seen in **Figure 2**.

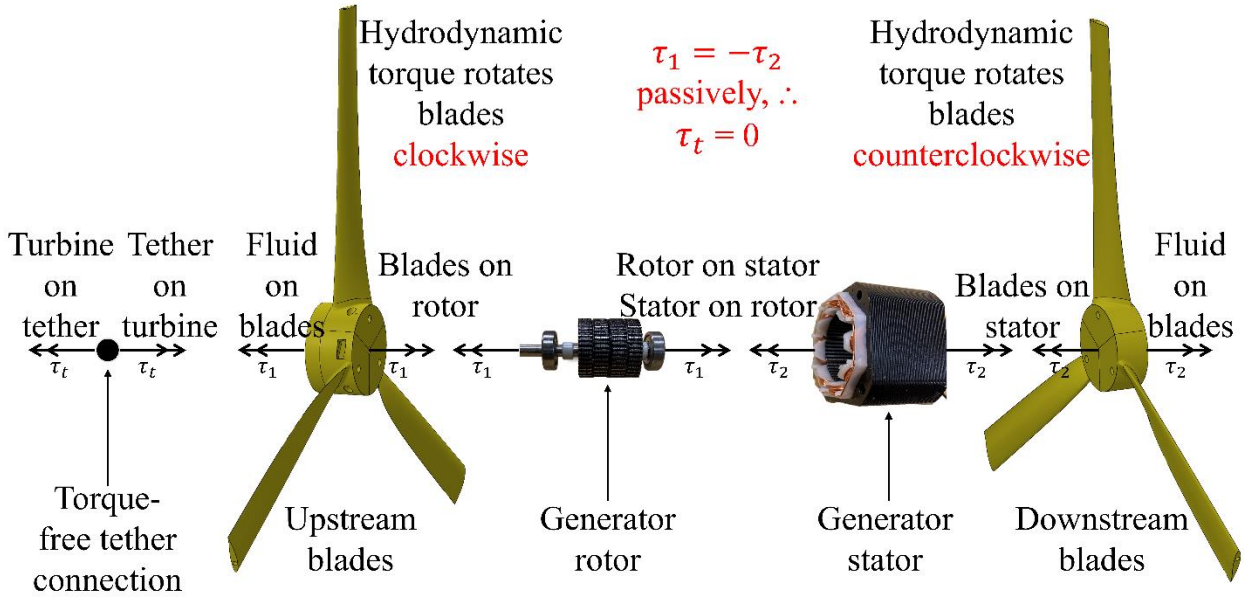

Figure 2. Simplified free body diagram of hydrodynamic and electromechanical forces in a direct drive counter-rotating hydrokinetic turbine demonstrating passive torque cancellation at steady state. Mechanical friction forces are neglected.

While this is a simplified model that neglects losses, it shows that during steady state conditions a mechanically simple and passive solution for torque cancellation is possible and thereby enables the use a of single-point tethering in a coaxial hydrokinetic turbine. This steady state assumption will be verified experimentally and will be discussed in section 3. Due to their equal magnitudes, all torques can be represented as the variable τ.

2.2. Selection of operating point using resistive load

The coefficient of power, C_P, has been shown to have a maximum of 0.59 for single rotors [25] and 0.64 for coaxial dual rotors [26]. To achieve maximum C_P for a variety of flow regimes, there must be a means of controlling the operating point of the system. The first way this can be

achieved is by controlling the hydrodynamic torque applied to both rotors. This can be accomplished by either changing the fluid velocity, which is not possible in an ocean current, or adjusting the pitch of the blades via actuators, which would increase complexity and cost. An alternative is to control the electromechanical reaction torque between the rotors by controlling the system via the generator. Assuming a DC generator and a resistive load, this can be done by prescribing the load resistance across the terminals of the generator or controlling the relative speed between the generator rotor and stator (e.g. via variable gearing). Considering these options, the generator load is chosen here to explicitly control torque for the sake of simplicity. For a fixed rotor design, it is desirable to study system response for a variety of flow speeds with constant load resistance. There is an infinite number of points at which this passive solution can be achieved, but there are several constraints that limit the range of torques within which these points can lie. First, the reaction torque between the rotor and stator must have a magnitude less than the maximum torque each rotor can generate hydrodynamically based on the blade geometry and local flow conditions. For each fluid velocity, the blade as a maximum thrust vector along the span that can be produced, directly limiting the maximum torque a set geometry is capable of. Next, it is assumed there is a one-way coupling in which the wake of the upstream rotor influences the output of the downstream rotor, but the wake from the downstream rotor does not impact the upstream rotor [27]. Therefore, the upstream rotor's torque output directly affects the downstream rotor's maximum torque production. For a DC generator, there is a range of rotor-stator reaction torques that are achievable. For a given rotor-stator relative speed, the maximum rotor-stator reaction torque occurs at the short circuit condition while the minimum occurs with an open circuit. The load resistance controls the relationship between rotor-stator relative speed and rotor-stator reaction torque, which determines the hydrodynamic torque that must be produced by both the

upstream and downstream rotors, that in turn correlates with a specific upstream rotational speed and downstream rotational speed. These are the equilibrium loci to be studied for each load resistance: cancelled torque magnitude, upstream rotational speed, and downstream rotational speed.

2.3. BEMT hydrodynamics model validation against water tunnel experiments

A method is proposed to find the equilibrium loci of torque cancellation based on Blade Element Momentum Theory (BEMT) with the addition of the Prandtl tip and hub loss factors for increased accuracy [28]. BEMT was not originally designed for dual rotors, but, using the one-way coupling assumption of upstream and downstream rotors [27], the standard BEMT formulation can be employed for the upstream rotor based on the method described by [29]. Once the result has been generated for the upstream rotor, the inflow velocity to the downstream rotor is defined as [27]:

$$v_{\infty,downstream} = v_{\infty,upstream}(1 - 2e_1) \quad (2)$$

where e_1 is the induction factor of the upstream rotor. BEMT outputs an induction factor for each discretized element along the span of the blades, so the average of these induction factors is used to create a singular e_1 value. This assumes a constant inflow velocity to each blade element of the downstream rotor, which is valid for a momentum disk, but in practice will not stand. However, this is a reasonable assumption for this analysis. The standard BEMT formulation can then be used for the downstream rotor using this inflow velocity.

This approach is applied, and the model is verified against experimental measurements from a lab-scale coaxial turbine experimental apparatus instrumented with electromagnetic brakes,

torque cells, and speeds sensors on each rotor and mounted to a rigid sting in the North Carolina State University Free Surface Water Tunnel as described in [24]. We consider the case when the turbine axis of rotation is aligned with the flow (i.e., zero skew angle). Our proposed model is applied to the turbine geometry and test conditions of [24] and the results are compared to the experimental measurements, shown in **Figure 3**. The data is also listed in **Table 1** to identify the pairings of upstream and downstream rotor speeds. The experimentally measured rotational speeds were used as the input to the model and the predicted torques are compared to the experimental torques measured. Cases where multiple torque values appear at the same downstream speed correspond to tests that had different upstream rotor speeds but the same reported downstream rotor speeds (to within the speed sensor resolution). With different upstream speeds, this affects the inflow velocity to the downstream rotor leading to different downstream torques even if they are measured at the same downstream rotational speed. The water tunnel offers a 81 cm wide x 71 cm x 244 cm long rectangular cross section test section, so in order to avoid any effects with the walls the prototype is a small scale, with a diameter of 20.32 cm, resulting in the low torque magnitudes seen in **Figure 3** and **Table 1**. The error bars represent the coefficient of variation as defined in [24]. A good agreement is observed between the experimental and proposed model prediction, thereby validating this model for use in this study.

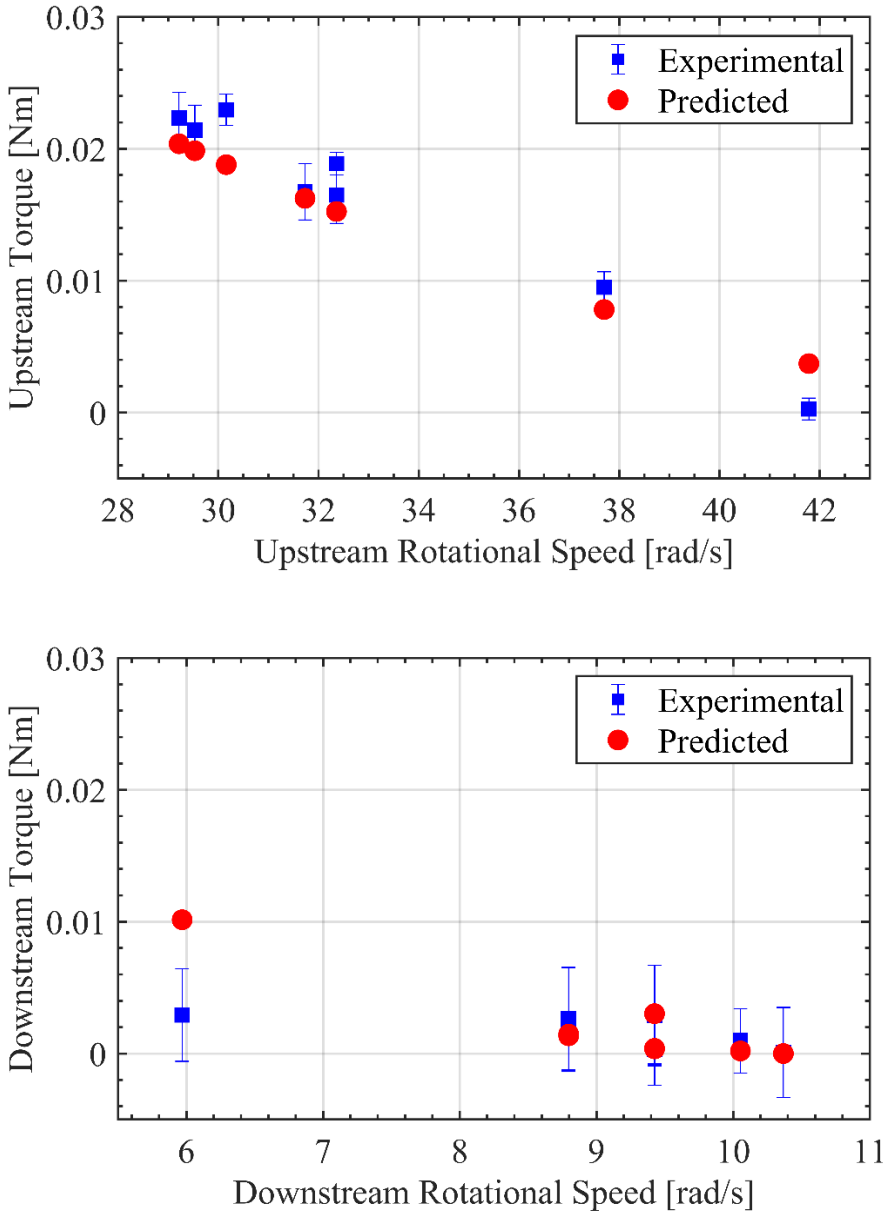

Figure 3. Comparison of BEMT prediction for coaxial turbine torque as a function of rotor speed to experimental data from Metoyer et al. [24] at 0.5 m/s for (a) the upstream rotor and (b) the downstream rotor.

Table 1. Each row represents one operating condition of upstream and downstream rotational speeds and measured torques at a flow speed of a v_∞ = 0.5 m/s.

Experimental Upstream Rotational Speed [rad/s]	Experimental Upstream Torque [Nm]	Predicted Upstream Torque [Nm]	Experimental Downstream Rotational Speed [rad/s]	Experimental Downstream Torque [Nm]	Predicted Downstream Torque [Nm]
29.22	2.232e-2	2.038e-2	9.43	2.962e-3	3.548e-4
29.53	2.140e-2	1.985e-2	9.43	2.893e-3	3.949e-4
30.16	2.296e-2	1.879e-2	10.37	8.062e-5	0.000
31.73	1.673e-2	1.624e-2	8.80	2.584e-3	1.345e-3
32.36	1.649e-2	1.524e-2	8.80	2.634e-3	1.475e-3
32.36	1.887e-2	1.524e-2	10.05	9.700e-4	1.967e-4
37.70	9.502e-3	7.806e-3	9.43	3.159e-4	3.026e-3
41.78	2.660e-4	3.705e-3	5.97	2.929e-3	1.015e-2

2.4. System definition

We consider a laboratory-scale coaxial turbine embodiment which has identical blades in both the upstream and downstream rotors for simplicity of design. The twist of the blades is selected based on the method described in [30], utilizing the optimal tip speed ratio for three blades, calculated to be $4\pi/3$ [31]. The twist is designed such that a straight rod can be inserted along the span of the blade, so the twist is calculated around this point. The SG6040 hydrofoil is selected for its performance at the low Reynolds numbers associated with an experimental apparatus of this scale and rotational speeds [32]. The experimental SG6040 coefficients of lift and drag data that

are used in our BEMT model are for Reynolds numbers of 100,000 – 500,000 [32], but there is deviation from this range near the hub. This portion of the blade does not contribute significantly to the torque generated by each blade, so this is deemed acceptable. Post-stall values of the coefficient of lift and coefficient of drag are included in the analysis. A constant chord of 3.125 cm along the blade span is chosen for an aspect ratio of approximately seven as a compromise between aerodynamic efficiency and structural rigidity. The rotor diameter of both upstream and downstream rotors is 50 cm, in-house fabrication capabilities. The rotors are spaced 25 cm apart, decided to test the 0.5D rotor spacing examined in [22]. The central hub diameter is 6.6 cm. An image of the physical system can be seen in **Figure 4**. While this embodiment is unoptimized, it provides a physical proof-of-concept and facilitates experiments to validate our model. Therefore, the parameters and component characteristics of this apparatus are considered in all of the analysis that follows.

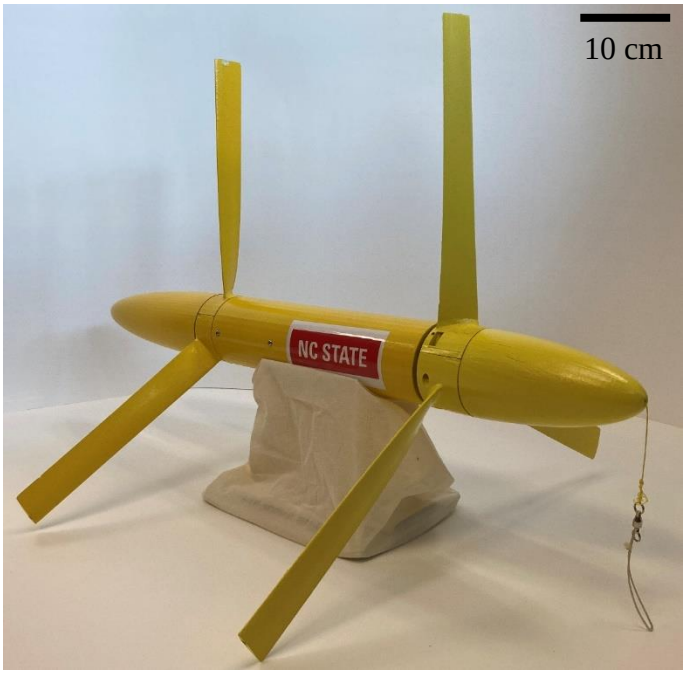

Figure 4. Assembled tethered coaxial turbine apparatus.

2.5. Solution method for theoretical torque-cancelling equilibria

With the geometry prescribed, the method begins by using BEMT to find the range of valid rotational speeds of the upstream rotor, ω_1. The minimum $\omega_1$is defined as the first ω_1 value where at least one of the 500 elements along the blade is not past the stall angle, estimated at 16 degrees [32], starting at $\omega_1 = 0.1\ rad/s$ and increasing by 0.1 rad/s until the condition is reached. The maximum ω_1 is subsequently found by starting at $\omega_1 = \omega_{1,min}$ and increasing by 0.1 rad/s until the last value of ω_1 before $C_P < 0$, using mechanical power to calculate the power extracted. This is demonstrated in **Figure 5(a)**. The quadratic shape of the C_P vs. ω_1 is due to the quadratic relationship between torque and rotational speed, seen in **Figure 5(b)**. This is derived from the fact that as the rotor increases its rotational speed, the proportion of the blade that is now rotating fast enough that elements of the blade are no longer stalled increases. This continues until the rotational speed where the maximum torque is extracted for a specific blade geometry. After this speed, parts of the blade go into stall and the torque begins to decrease. The reason that some elements enter/exit stall before the others is while the rotational speed of the entire rotor is constant, but the tangential velocity increases along the span toward the tip. The relative velocity seen by each element is the vector sum of inflow velocity and tangential velocity at that radial position, each corrected for the axial and tangential induction factors at this element [29]. This relative velocity seen by each element defines the angle of attack of that element, determining if it is in stall or not. **Figure 5(b)** is interpreted to imply that for any reaction torque to the upstream rotor, the system can come to rest at two different ω_1. Intuition tells us that one of these ω_1 points should be stable, and one should be unstable. To examine which point is stable, the hydrodynamic torque must be compared to any potential reaction load torque. If τ_1 is greater than the reaction torque,

then the angular acceleration of the upstream is positive, and ω_1 will increase. Contrarily, if the reaction torque is greater than τ_1, then the angular acceleration is negative, and ω_1 will decrease. With this knowledge, all ω_1 on the left-hand side of the apex of the curve of **Figure 5(b)** will be unstable because to the left of any point on this side of the curve, any perturbation that decreases τ_1 to be less than the reaction torque will cause ω_1 to decrease, and any perturbation that increases τ_1 to be greater than the reaction torque will cause ω_1 to increase. Any perturbation will cause a divergence from points on the left-hand side of the curve. Conversely, all ω_1 on the right-hand side of the apex of the curve of **Figure 5(b)** will be stable because to the left of any point on this side of the curve, any perturbation that decreases τ_1 to be less than the reaction torque will cause ω_1 to decrease, and any perturbation that increases τ_1 to be greater than the reaction torque will cause ω_1 to increase. Any perturbation will cause a convergence to points on the right hand side of the curve.

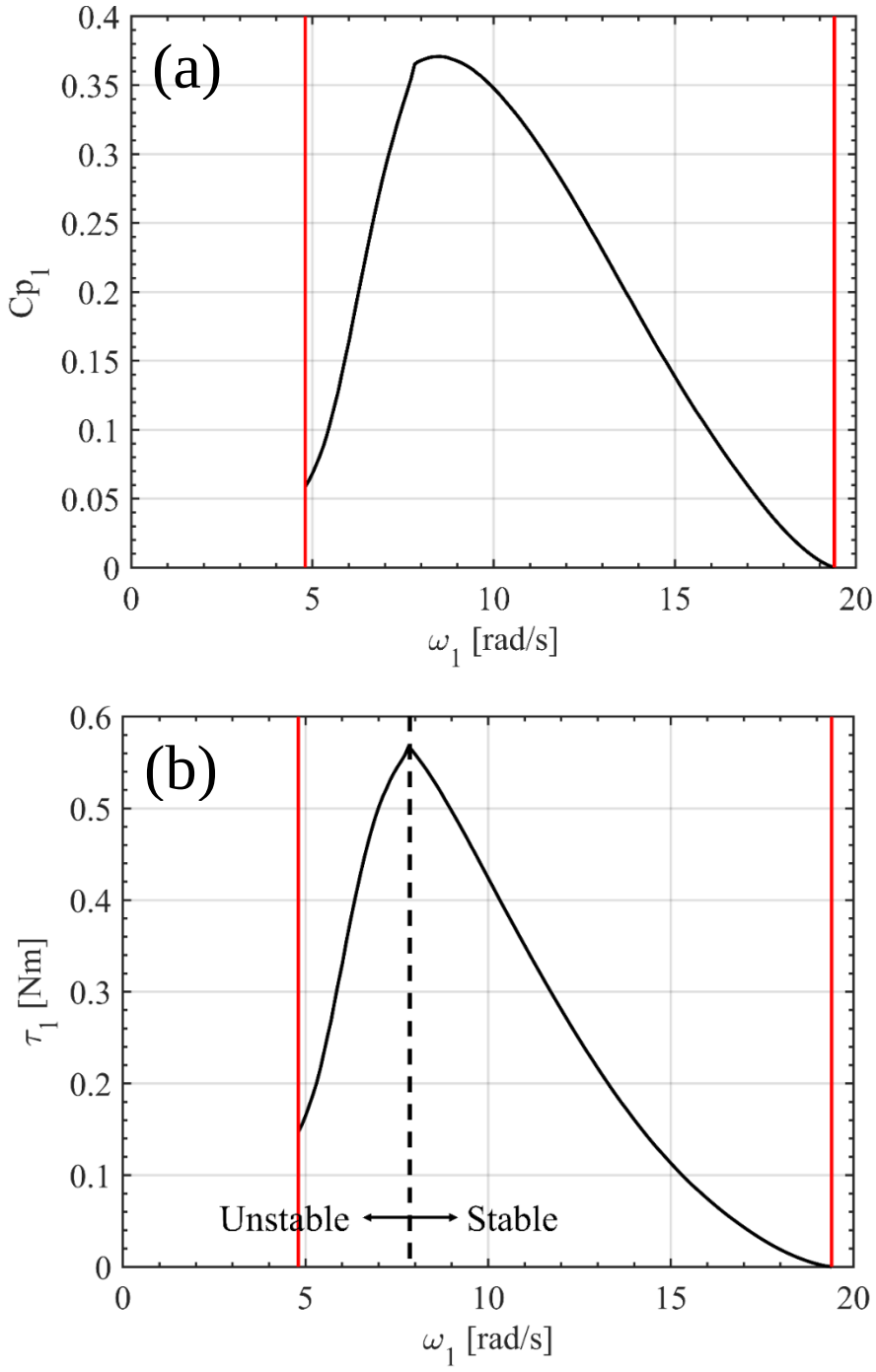

Figure 5. (a) C_p as function of upstream rotor when swept through values of ω_1 for v_∞ of 0.5 m/s. (b) Upstream torque when swept through values of ω_1 for v_∞ of 0.5 m/s. Red, solid vertical lines represent the valid range of ω_1 where the blades are not completely stalled and give a positive C_p value. Dashed vertical line represents point when ω_1 changes from unstable to stable.

The same procedure is used to find the minimum speed of the downstream rotor, ω_2. It was found through extensive analytical testing that the maximum ω_2 can be set to the same maximum as ω_1 and provide a valid range for all domains of interest, a simplification that significantly reduces computation time. This valid range of ω_1 and ω_2 is then discretized into 500 equally spaced values. For each ω_1, the range of all discretized ω_2 is run through the BEMT algorithm. The corresponding torques associated with the given ω_1 and swept ω_2 values are shown in **Figure 6**. The goal is to identify ω_2 values that correspond to torques equivalent in magnitude while rotating in opposite directions. Those results that satisfy the following conditions are considered valid:

- The result must not violate momentum theory for an energy extraction device, namely the induction factors, $e_1$and e_2, must both be positive. Positive inductions mean both rotors are extracting energy rather than inputting energy to the flow as expected for a turbine.
- Both $e_1$and e_2 must be less than 0.5, a value which, if exceeded, implies flow reversal and known fallacy [33].

Any points that do not meet these criteria are deemed invalid and are not recorded. Intersection points of the two curves of **Figure 6** reveal the ω_2 values that correlate to the same magnitude τ generated by the upstream rotor. These specific curves were calculated for an upstream rotational speed of 15 rad/s and a v_∞ of 0.5 m/s into the upstream rotor, yielding an e_1 of 0.23, resulting in an inflow velocity of 0.27 m/s into the downstream rotor. The curve of downstream torque begins at the first ω_2 value that at least one element of blade is not stalled. The upstream torque is constant due to the coupling assumption that the downstream rotor does not affect the behavior of the upstream rotor, so the upstream torque remains unchanged for all values of ω_2. Arrows denote the stability analysis of the downstream rotor. If the downstream torque is greater than the upstream

torque, acting as the reaction torque to the downstream rotor, then the angular acceleration will be positive, causing the downstream rotor speed to increase. If the downstream torque is greater than that of the upstream, then the angular acceleration will be negative, and the downstream rotor speed will decrease. This implies that the lower downstream rotational speed is unstable due to the downstream rotor diverging from this point in the case of any perturbations. Conversely, the downstream rotational speed is stable due to the converging response to perturbations.

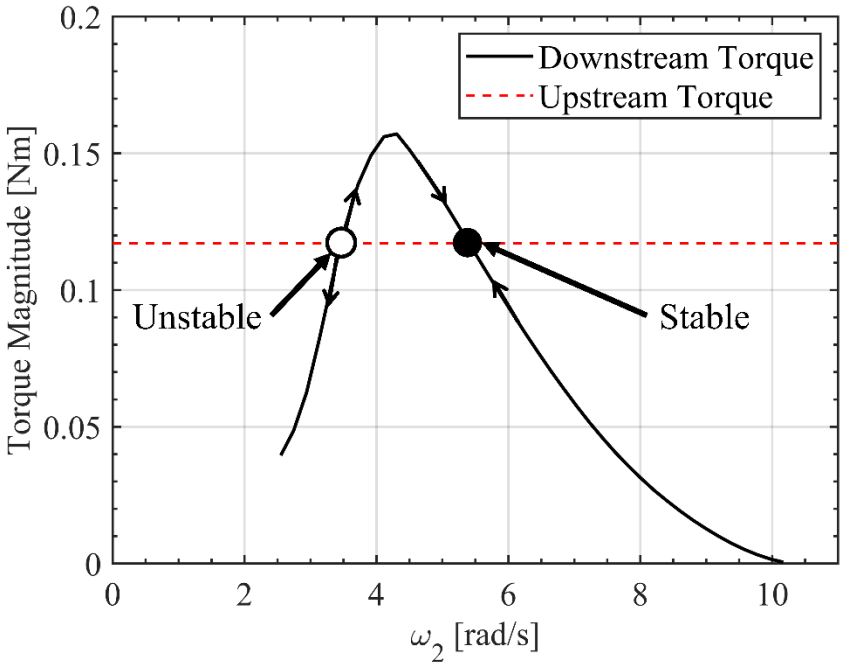

Figure 6. Intersection of upstream and downstream torque for a specific upstream rotation speed. Here, ω_1 = 15 rad/s and v_∞ = 0.5 m/s into the upstream rotor.

This process has been repeated for a range of v_∞ from 0.2 m/s to 0.8 m/s, increasing by 0.1 m/s each loop. For each v_∞, all (ω_1, ω_2) pairs that allow the downstream rotor to generate the same torque magnitude as the upstream rotor, τ, are recorded. This creates a table of equilibrium loci points (τ, ω_1, ω_2) at each of the seven v_∞ examined. Once these values are found, the resistive

load that imposes these operating points is determined. For a DC generator, the following relationships are known [34]:

$$iR_{load} = -iR_{arm} + K_e(\omega_1 + \omega_2) \quad (3)$$

$$\tau = K_\tau i \quad (4)$$

where i is the current, R_{load} is the load resistance across the generator's terminals, R_{arm} is the armature resistance of the generator, K_e is the back-emf constant of the generator, and K_τ is the torque constant of the generator. R_{arm} was measured to be 2.1 Ω for the hardware embodiment considered here. In DC generators, the K_e and K_τ are equal in SI units. Rearranging Eq. (3) and (4), the necessary R_{load} to prescribe the theoretically calculated loci is calculated as:

$$R_{load} = -R_{arm} + \frac{K_e K_\tau}{\tau}(\omega_1 + \omega_2) \quad (5)$$

A stepper motor is used as the generator for this system, the reasoning for which is described in section 2.6. To experimentally find K_e, a system is developed that can prescribe a rotational speed to the selected generator and the induced voltage across a known load resistance is measured. A bridge rectifier is added to each output of the stepper motor, a capacitor is placed across the bridge rectifier outputs, and these outputs are put in series to create a singular load voltage that is measured. This system can be seen in **Figure 7**.

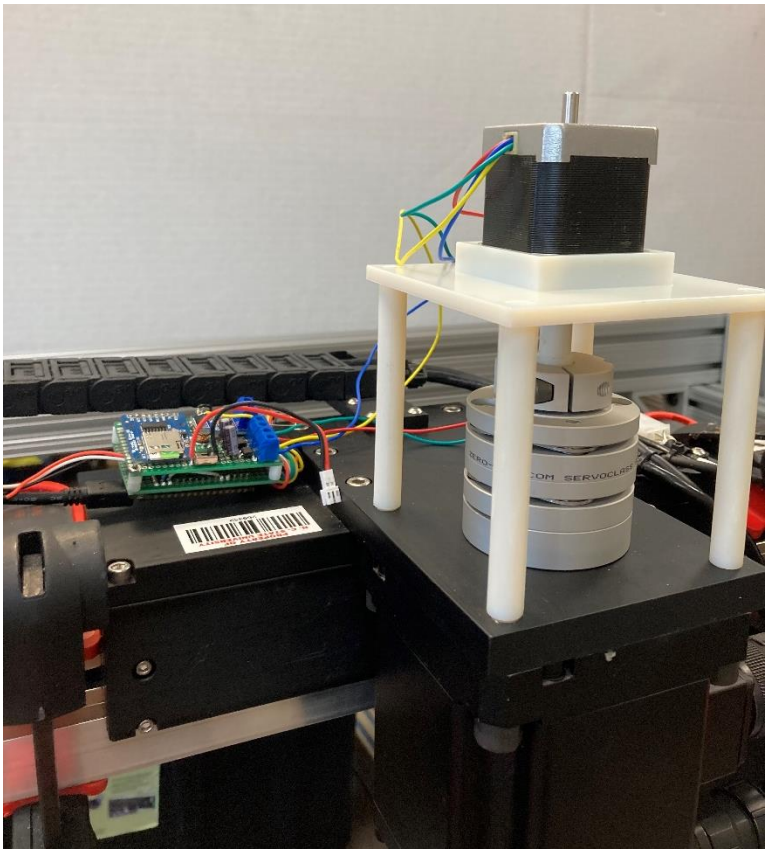

Figure 7. Motor constant experiment setup.

With the data from this motor constant experiment, Eq. (3) is rearranged to solve for K_e:

$$K_e = \frac{V_{peak} + (\frac{V_{RMS}}{R_{load}})R_{arm}}{\omega_1 + \omega_2} \quad (6)$$

This creates an "effective back-emf constant" of the stepper motor and bridge rectifier system. The rotational speeds that were measured during the pool tow testing, to be described later, are used as the input speeds and the load resistances used during the pool tests are used in this experimental method. All values of K_e found by Eq. (6) are averaged to create a constant K_e to be used to find the experimental torque and to be used in the model. The averaged value is found to be 0.423.

With the model completed, a table comprising of the equilibrium loci is generated to create an equilibrium loci frontier. Next, this table is used in conjunction with the MATLAB function

'*fmincon*' as the initial guesses of ω_1 and ω_2 to find the equilibrium loci values at the specific, desired R_{load} values tested experimentally: 250 Ω, 500 Ω, 750 Ω, and 1000 Ω. This process is repeated for the four v_∞ that are tested experimentally: 0.47 m/s, 0.57 m/s, 0.67 m/s, and 0.77 m/s. These are the specific predicted operating points that will be compared to the experimental values.

2.6. Construction of experiments to demonstrate equilibrium loci trends

The experimental apparatus pictured in **Figure 4** is used to confirm the model-predicted trends in torque-cancelling equilibria. The blades, nacelle, and nose and tail cone shells are fabricated via a Stratasys Objet 30 3D printer. Expanding polyurethane foam is used to fill the nose and tail cones to adjust buoyancy. The nose cone profile is elliptical with a fineness ratio of two, deemed the optimal for subsonic vehicles [35]. Because the generator is located forward at the leading set of blades as shown in **Figure 9**, ballast is required aft to trim the turbine longitudinally so the center of gravity (CG) and center of buoyancy (CB) are collocated. A 100g ballast mass of tungsten putty and BB pellets was affixed at the tip of the tail cone before foam was added, and an elongated elliptical tail cone with a fineness ratio of three is selected to give a greater moment arm to move the CG farther with less required ballast. The blades are stiffened with a carbon fiber rod inserted spanwise and epoxied in place. The upstream blades, which spin clockwise, are fixed to the shaft of the generator via a dowel pin that runs through a hole drilled perpendicular to the axis of rotation of the generator shaft. This pin then fits into a channel in two of the blades. The blades are then secured to each other, so the hydrodynamic torque acting on the blades is transferred to the generator shaft through the dowel pin. A 3D printed jig was used to secure the generator shaft from rotating when using the drill press to create the hole in the generator

shaft, along with a guide in the 3D printed part to assist in centering the hole in the center of the shaft. Any offset in the hole location was found to cause oscillations in tow testing. This setup can be seen in **Figure 8**.

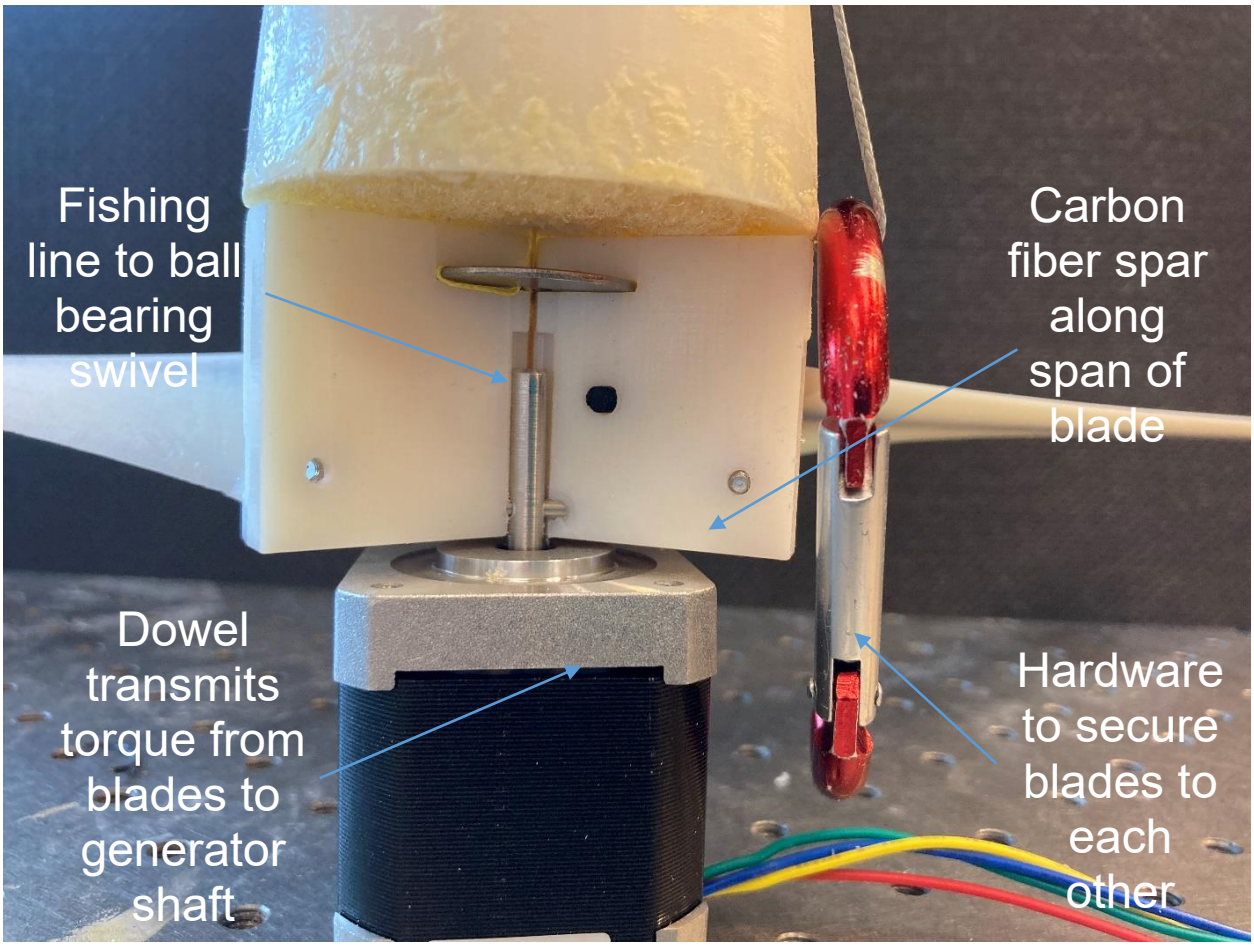

Figure 8. Assembly of upstream blades to generator rotor.

The downstream blades are fixed to the housing nacelle and generator housing to spin the stator counterclockwise via a spline between the downstream blades and nacelle. A commercial, dual shaft, off-the-shelf stepper motor is selected as the generator to produce a high voltage output as compared to other brushless variants, producing more distinguishable differences in power

production between test cycles. However, a brushless style is still desired, as it permits complete submersion without shorting. The specific motor purchased was a NEMA17 from CNCTOPBAOS, model 17HS8401B. It should be noted that a generator is the inverse equivalent to a motor, and it is standard to use motors as generators [36]. Stepper motors produce two AC voltages, while the theoretical approach is based on DC configurations. This is addressed by adding full bridge rectifiers to both AC outputs. Capacitors placed in series across the bridge rectifiers terminals yield a more constant output while simultaneously combining the two AC outputs into a single DC voltage. During testing, the downstream rotational speed relative to the fixed reference frame is measured by an inertial measurement unit (IMU) located in the nacelle, and the relative rotational speed between the upstream and downstream rotors is measured by a Hall sensor and eight magnets spaced around the circumference of a plate fixed to the rear shaft of the generator. A voltage sensor is used to measure the voltage across the load and the RMS value, V_{RMS}, is calculated from this data. Using the V_{RMS} calculated and the known R_{load}, Ohm's Law is used to define the i generated during test. Eq. (4) can then be solved for τ to compare to the theoretical modeling. This method was chosen to measure the torque due to their being no stationary element on the turbine against which to measure a reaction torque. In order to differentiate each test, a clock is added onboard. The starting and ending time of each test is recorded by the researcher and is then correlated to a timestamp the clock attaches to each data point logged onboard. An exploded view of the design can be seen in **Figure 9**.

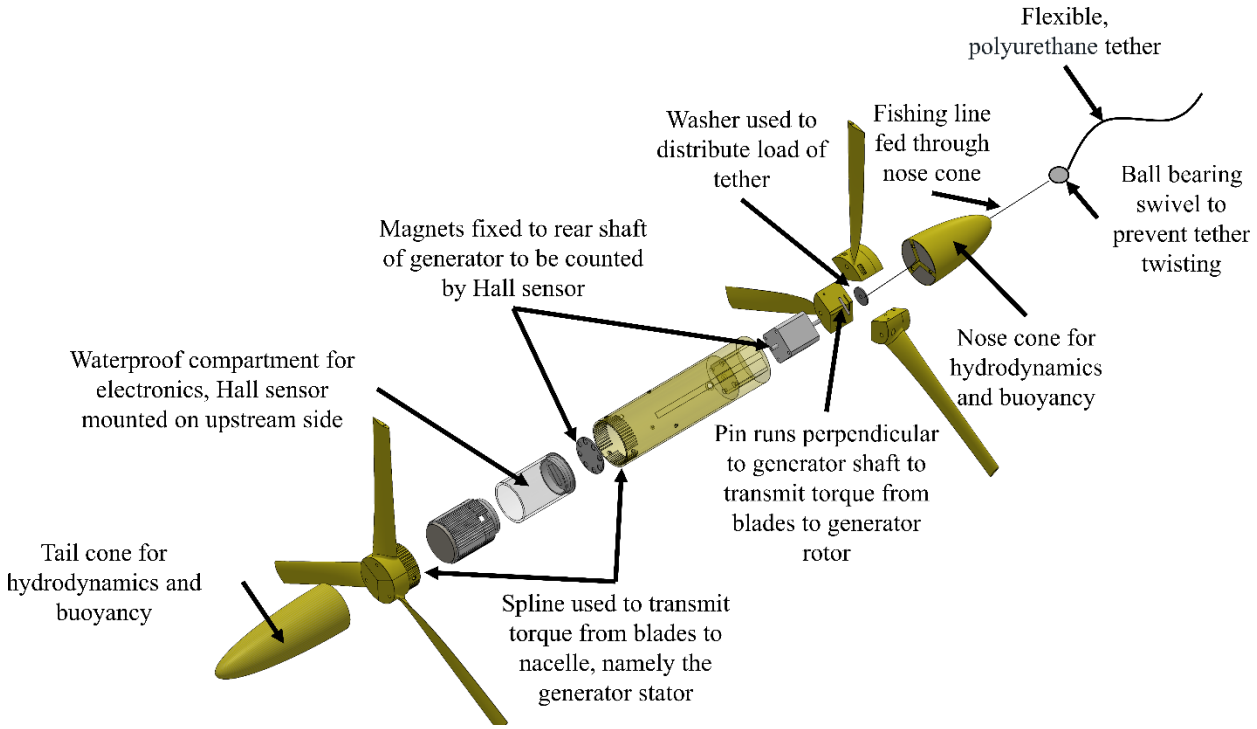

Figure 9. Exploded 3D model with callouts to show assembly of experimental apparatus.

The experimental apparatus is towed on a tether across the diving well of the North Carolina State University 25-Yard Swimming Pool under closed-loop winch control. The towing winch system pulls a floating raft across the surface with the coaxial turbine apparatus connected by a 3 m flexible, polyurethane tether. To fix the turbine to the tether, fishing line is attached to a washer that fits in a cutout in the center of each of the upstream blades. When the blades are secured together, the fishing line is run through a channel in the nose cone and is tied to a ball bearing fishing swivel that allows the upstream rotor to rotate without twisting the tether. The swivel is attached to a carabiner which attaches to the end loop of the tether on the tow system. The turbine is trimmed to operate at approximately zero skew angle and the tether is attached approximately 2 m below the underside of the raft by a rigid rod cantilevered from the raft. This system is described in **Figure 10**.

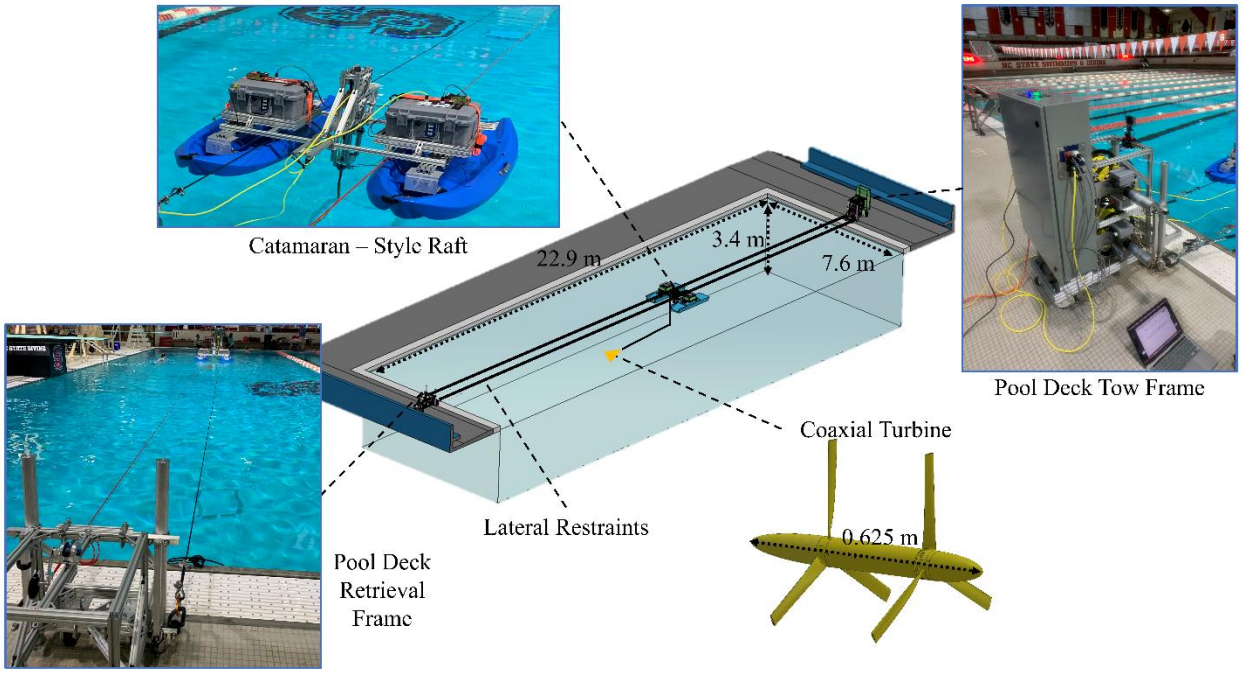

Figure 10. Experimental tow system utilized to simulate a variety of v_∞.

Data is collected by an onboard Arduino Nano microcontroller utilizing the aforementioned sensors the turbine was towed for a constant R_{load}. All except the Hall sensor were sampled at 100 Hz. To increase accuracy for the Hall sensor, the time span to count 100 magnet passes is measured. This process is repeated for four distinct v_∞ ranging from 0.47 m/s to 0.77 m/s, values determined by the experimental setup. The R_{load} is then changed and the same four fluid velocities are tested at this new R_{load}. An image of the turbine apparatus being towed by the experimental system can be seen in **Figure 11**.

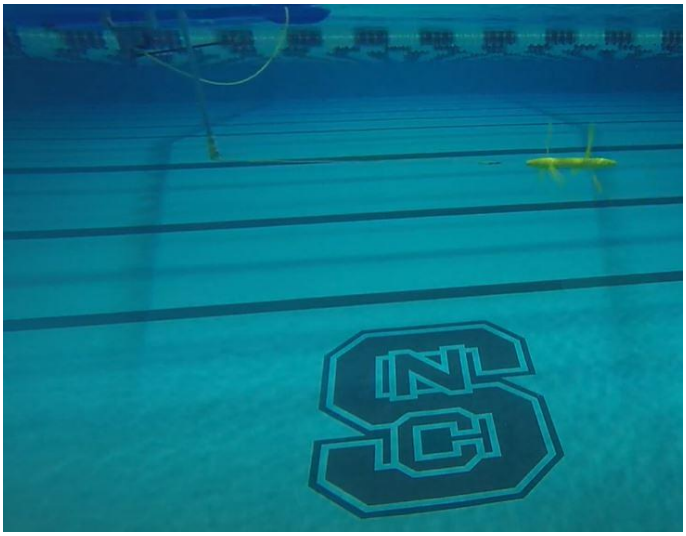

Figure 11. Experimental apparatus being towed across NC State pool at constant speed to mimic constant fluid velocities.

3. Results and Discussion

The theoretical modeling is implemented and a frontier of equilibrium loci of ω_1, ω_2, and τ were found. These points are plotted in **Figure 12** projected onto a two-dimensional plane.

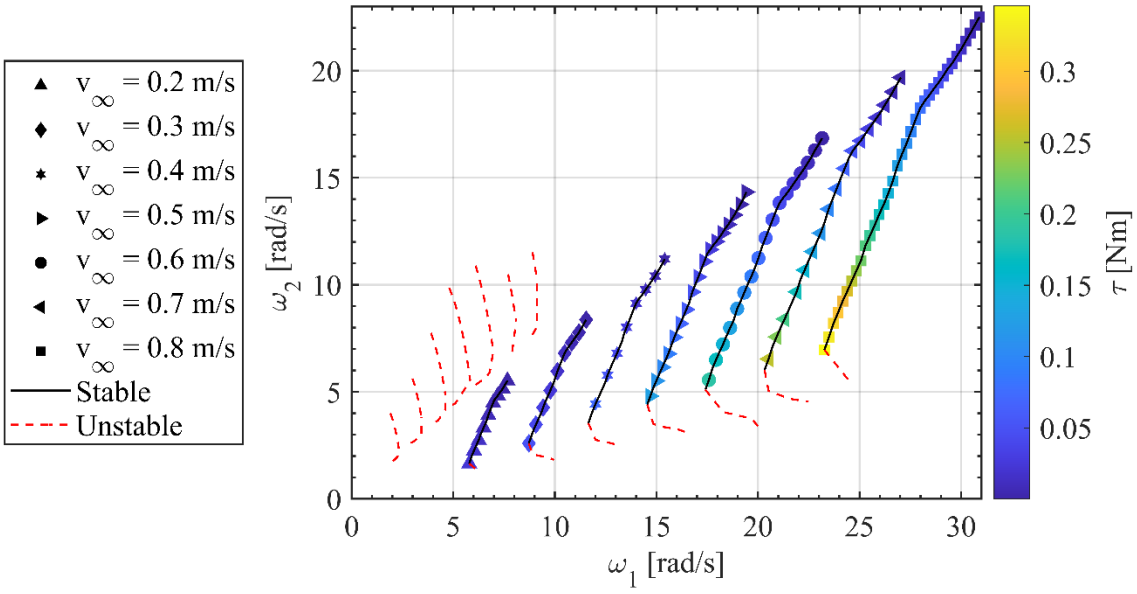

Figure 12. Equilibrium loci frontier of model-predicted torque-cancelling operating points found by sweeping through possible values and recording those that meet stated criteria. Only stable loci points are plotted with corresponding torque magnitude in color scale, unstable points are denoted as the dashed red line on the ω_1, ω_2 plane.

The first observation from **Figure 12** is the trends of the equilibrium stability analysis presented in section 2.5. As seen in **Figure 6**, the stable points are associated with the higher values of ω_2, with the stable and unstable points for each ω_1 creating a vertical parabola shape for each v_∞. The next observation is that there are ranges of ω_1 where the downstream rotor cannot generate an equivalent magnitude τ for any valid ω_2. The upstream rotor extracted enough energy from the flow that the rear rotor cannot produce the same torque from the limited energy remaining in the upstream rotor's wake. The equilibrium loci are located at the extrema of the range of valid ω_1 for all v_∞. The next trend observed is that an increase in v_∞ gives a larger range of ω_1 so the curves are shifted outward along the ω_1 axis for the upper extrema ω_1 values and inward for the lower extrema ω_1 values. However, the trends remain the same for each v_∞. The curves are increasing

in scale as v_∞ increases, increasing the maximum τ magnitude feasible for this configuration. It is noticed that lower ω_1 correlate to larger magnitude τ when compared to the higher ω_1 curve for the same v_∞, a trend that follows conventional motor logic that lower speeds correlate with higher torque. Finally, it is seen that $\omega_1 > \omega_2$. This was counter intuitive when thinking about equal magnitude torques, but the reason is that due to the induction of the upstream rotor, the downstream rotor is in a different flow regime than the upstream, so the rotational speeds of each should be different. Each of the points in **Figure 12** corresponds to a specific R_{load} that is calculated from Eq. (5).

In the experiment, R_{load} is held constant at values of 250 Ω, 500 Ω, 750 Ω, and 1000 Ω. The corresponding equilibrium loci to these R_{load} are found and are in **Figure 13**.

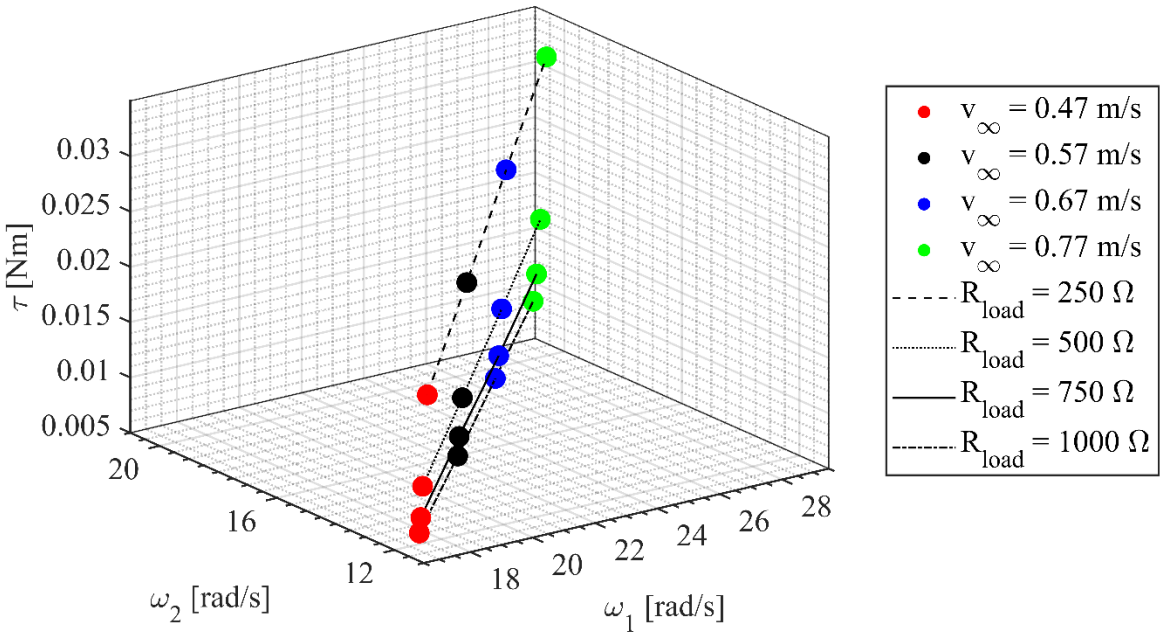

Figure 13. Equilibrium loci of ω_1, ω_2, and τ for four increasing v_∞ for a constant R_{load} of 250 Ω, 500 Ω, 750 Ω, and 1000 Ω.

Figure 13 demonstrates the equilibrium operating conditions of the coaxial turbine with constant load resistance for four different v_∞. It is noted that lower values of R_{load} generate higher torques. While this is an expected trend in motors and generators with prescribed speed, it was unknown whether the hydrodynamic coupling between rotor speed, torque, and induced flow with support this trend in the equilibrium operating points of the coaxial turbine. The magnitude of ω_1 and ω_2 values are relatively constant for all values of R_{load}, only the torque magnitude differs between the R_{load} values significantly. Given the nonlinearities seen in **Figure 12**, this is an interesting observation.

These observations from the theoretical modeling are then compared to the experimental trends. During the experiments, a video camera is placed along the span of the pool to qualitatively examine the stability of the system. The experimental apparatus was designed to be approximately neutrally buoyant and have the CG and CB to be radially located on the axis of rotation. It was observed that when the system was either negatively buoyant or if the CG and CB were not both located on the axis of rotation there were visible oscillations. When the system was corrected to return to approximate neutral buoyancy or to relocate the CG or CB, there were minimal oscillations. The ω_{rel} measured during the experiment for R_{load} = 1000 Ω is plotted in **Figure 14**. Minor oscillations are seen and are derived from minute differences in CG and CB radial locations, but the plateau seen after the test is initialized confirms the steady state assumption from section 2.1. This transient data is removed, and the remaining data is averaged to estimate an experimental value of each equilibrium loci for each test. Due to the constant pool length seen in **Figure 10**, as the tow speed is increased the duration of each test decreases. The raft stopping point varied slightly between tests, so this decrease in testing time as tow speed increases is not constant between tests. Other values of R_{load} exhibit similar trends in ω_{rel} with time.

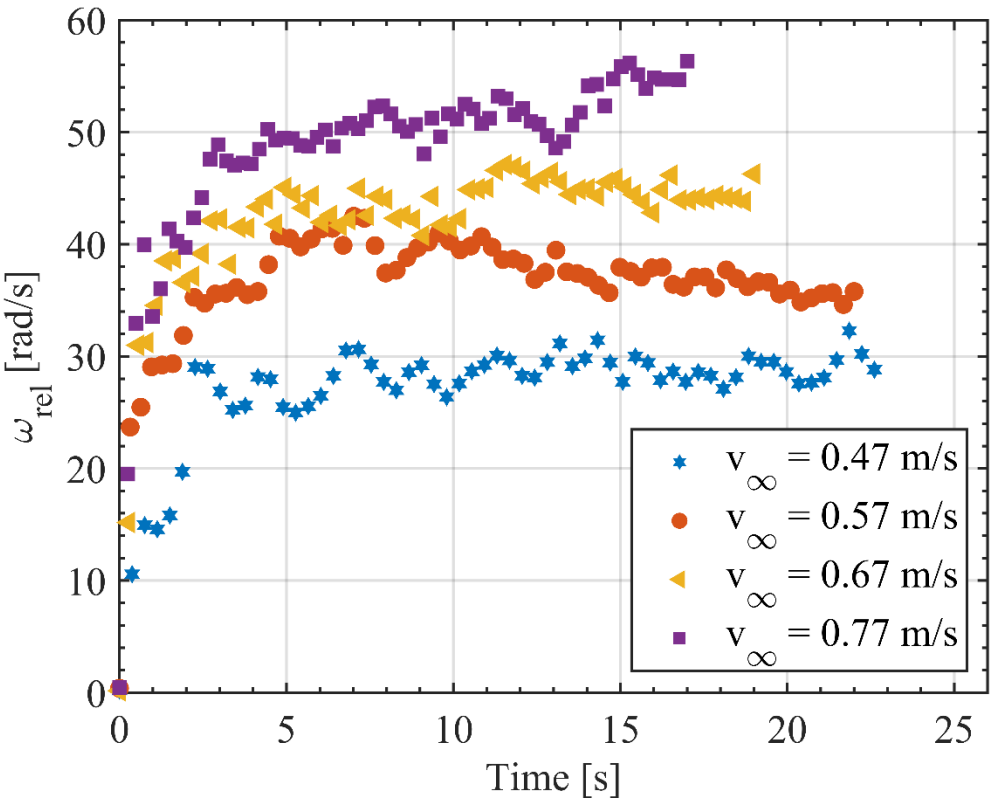

Figure 14. Relative velocity between generator stator and rotor measured for one R_{load}. The steady state assumption for torque cancellation is verified by the trend of the data plateauing after initial transients.

The onboard measurements from the experimental apparatus following the aforementioned averaging procedure and corresponding comparisons to the theoretical predictions can be seen in **Figure 15**, **Figure 16**, and **Figure 17**. The theoretical predictions are based on the true values of R_{load} from the true resistor values, namely 250 Ω, 515 Ω, 752 Ω, and 982 Ω.

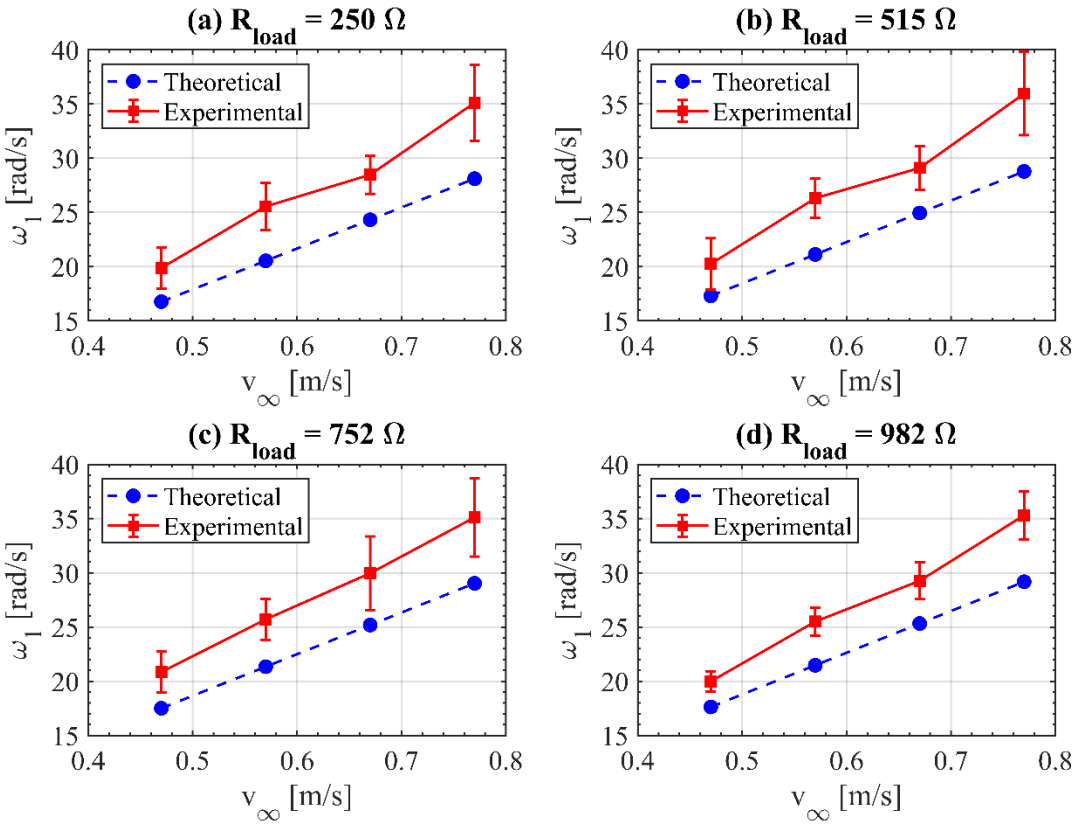

Figure 15. Comparison of theoretical values to experimental measurements of equilibrium locus of ω_1 for a constant R_{load} of (a) 250 Ω, (b) 515 Ω, (c) 752 Ω, and (d) 982 Ω. Error bars indicate one standard deviation of data collected.

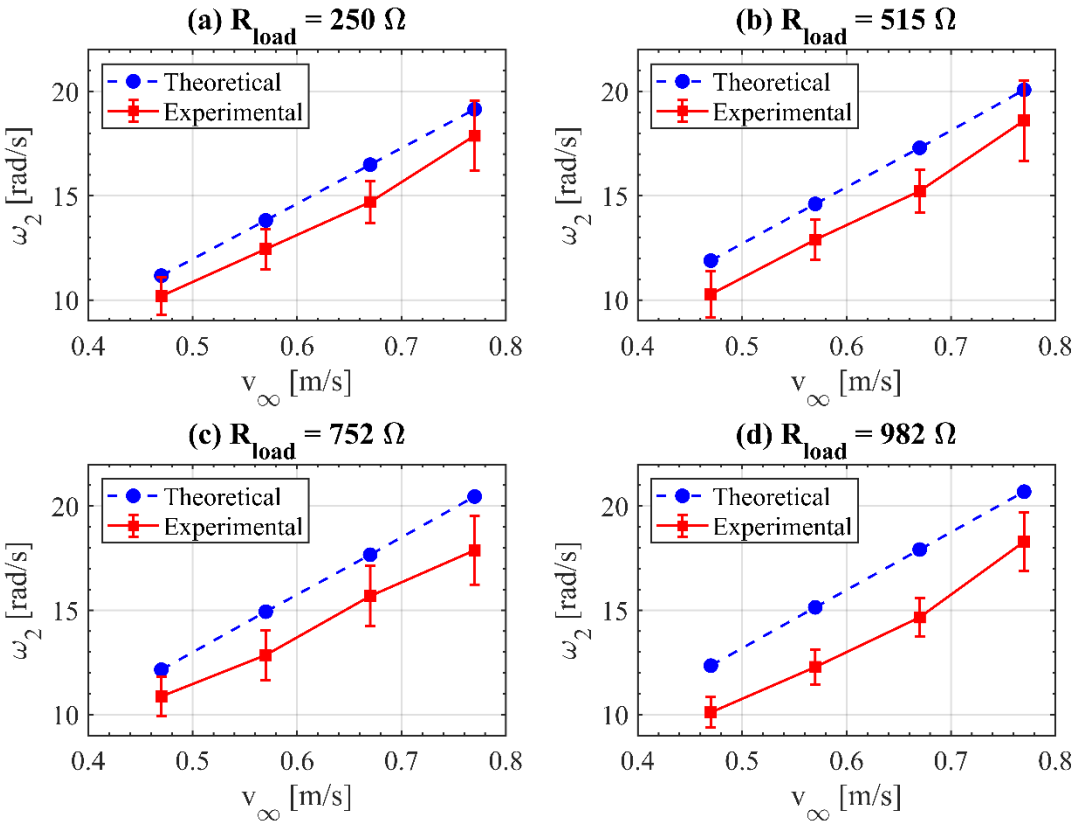

Figure 16. Comparison of theoretical values to experimental measurements of equilibrium locus of ω_2 for a constant R_{load} of (a) 250 Ω, (b) 515 Ω, (c) 752 Ω, and (d) 982 Ω. Error bars indicate one standard deviation of data collected.

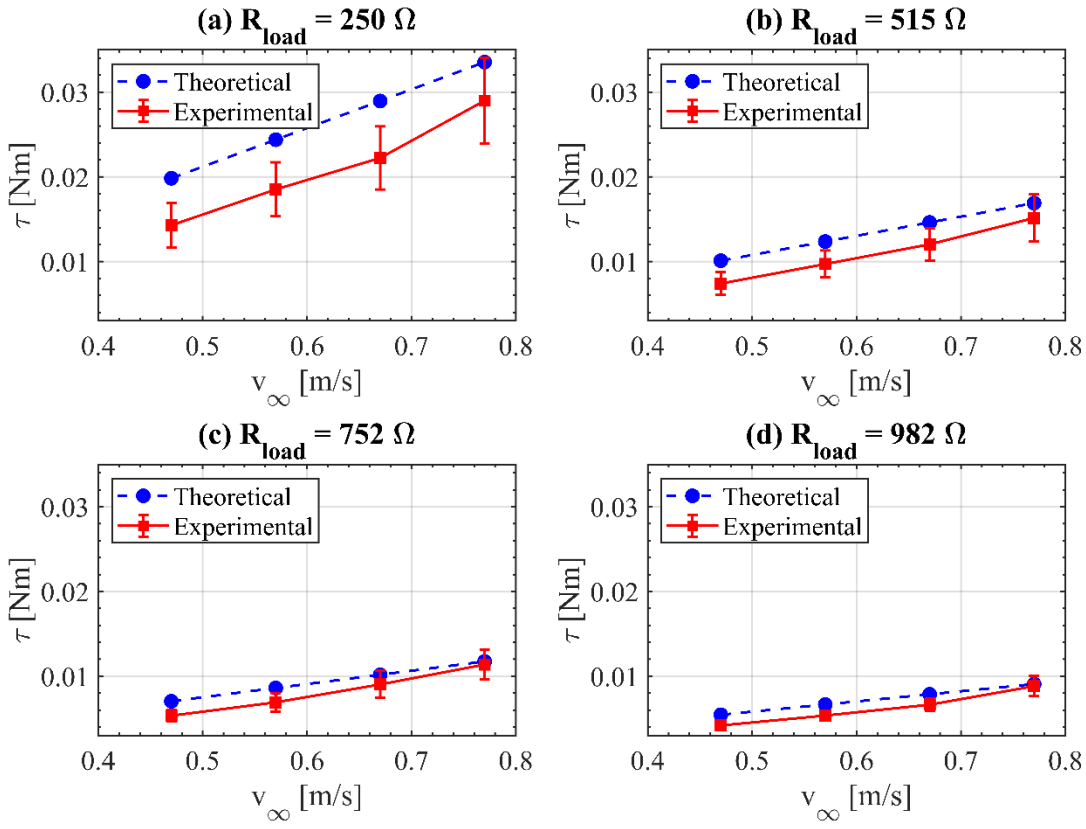

Figure 17. Comparison of theoretical values to experimental measurements of equilibrium locus of τ for a constant R_{load} of (a) 250 Ω, (b) 515 Ω, (c) 752 Ω, and (d) 982 Ω. Error bars indicate one standard deviation of data collected.

The trends are approximately linear for all R_{load} values and for all equilibrium loci parameters, and approximately the same magnitude of ω_1 and ω_2 is seen for all R_{load} values. This confirms the trends theoretically predicted from **Figure 13**. This linearity is intuitive for rotational speeds but is nonintuitive for torque. While torque varies as the square of rotational speed hydrodynamically, torque varies linearly with rotational speed in DC generators with constant resistive load. The trends of the generator supersede the hydrodynamic because the linear trend of torque versus speed is required of DC generator operation, while portions of the upstream and

downstream rotors can be forced to stall to reduce the quadratic increase with v_∞ to a linear increase that is imposed by the generator and electrical load condition.

Figure 17 demonstrates that the model overpredicts the torque to be generated, which would then correlate with lower rotational speeds than would be observed experimentally. This is true of the upstream speed, seen in **Figure 15**, but is not the case in **Figure 16** for the downstream rotor. This can be reconciled knowing that ω_1 is higher than the model, leading to a larger induction factor of the upstream rotor compared to the model's prediction. This higher induction factor leads to a decreased inflow to the downstream rotor, so a decreased rotational speed of the downstream rotor is required to generate the equal torque of the upstream rotor, even though the torque required to be generated experimentally is less than was theoretically forecast.

While there is good correlation, there is a deviation from the model to experimental values. The difference between the model and experiments has several potential sources: surface finish imperfections of the blades, hydrodynamic losses that are not modeled, motor constants that deviate slightly from supplier specifications, and friction of the generator bearings that are not modeled. However, the same previously unknown trends seen analytically are also seen experimentally, giving confidence in the model.

This now lends to the model being used to predict the preferred R_{load} for maximum energy extraction, namely the maximum C_P. The model's predicted C_P, calculated by Eq. (1) with P being mechanical power, is shown in **Figure 18** as the v_∞ increases utilizing a constant R_{load} and geometry.

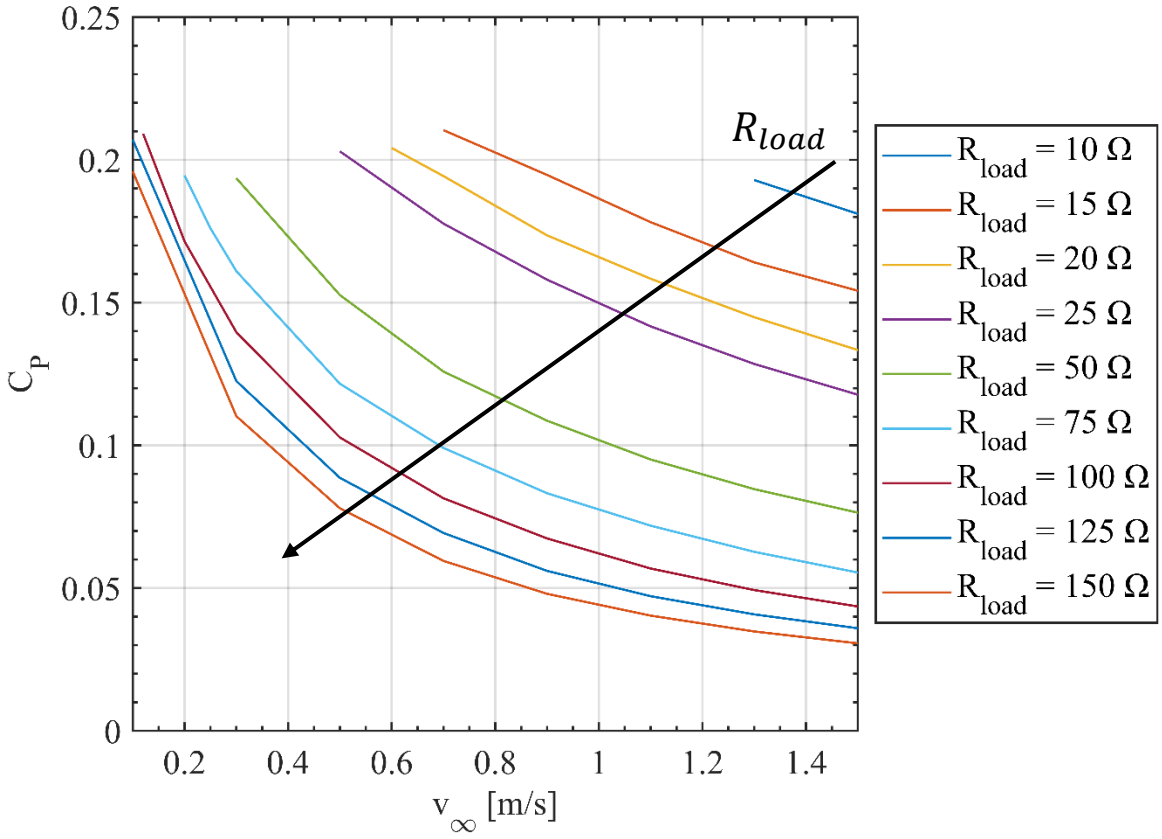

Figure 18. Model-predicted C_P of coaxial turbine apparatus using direct drive counter-rotating generator with constant R_{load} show that lower resistances yield higher power extraction over a variety of flow speeds. However, as R_{load} decreases, the minimum v_∞ required to generate a torque cancelling operating point increases.

Figure 18 illustrates that the proper selection of R_{load} can yield a greater energy extraction for a constant fixed geometry. The downward slope in C_P while v_∞ increases implies that while the power available in a flow increases cubically with v_∞, the power extracted is not increasing at the same rate. Based on the linear trends of rotational speed and torque, this would imply power extracted increases quadratically with v_∞, causing the decreasing C_P as v_∞ increases. While the increments of R_{load} scale linearly, their effect on C_P is nonlinear. This is seen in the larger increase in C_P between a R_{load} of 25 Ω to 50 Ω than the increase in C_P between a R_{load} of 50 Ω to 75 Ω.

For the lowest values of R_{load} at the lowest fluid velocities, the model predicts that no torque cancellation equilibrium loci exist, correlating physically to the system not rotating. This indicates that the lower values of R_{load} achieve higher C_P values, but at the expense of range of feasible fluid environments, and the model can be utilized to explore this tradeoff. If the lower v_∞ are the most prevalent that the coaxial turbine is exposed to, then a R_{load} that can at least perform at these values should be chosen. If is the coaxial turbine is seldomly exposed to such low velocities, a R_{load} that generates the greatest C_P most of its operational window and dormant for the remaining time is preferred to a R_{load} that generates a lower C_P for the entirety of the v_∞ window.

While the modeling can show the general magnitude of the R_{load} necessary, the physical system must be redesigned to accomplish these results. Currently, the geometry of the blades has not been optimized, the geometry of the upstream and downstream blades could be different since the downstream blades are exposed to a different flow regime than the upstream blades, and the friction of the generator bearing could be decreased to assist in meeting these predictions.

4. Conclusion and Future Work

4.1. Conclusions

Hypothesizing that a single generator can be used as a coupling between the upstream and downstream rotors of a coaxial turbine to passively cancel torque at steady state, a model is derived and compared against tow-test experiments with a laboratory-scale coaxial turbine. The loci of model-predicted and experimentally-observed equilibrium rotor speeds and generator torque show good correlation as freestream flow speed and load resistance are varied. The model and

experimental results also illustrate several findings: First, the same magnitude of upstream and downstream rotational speeds is seen for each freestream fluid velocity regardless of the load resistance, with only the magnitude of the torque varying with a change in load resistance. Next, a linear relationship between fluid velocity and all three equilibrium state variables, namely upstream rotational speed, downstream rotational speed, and torque magnitude, is observed. Finally, lower values of load resistance correspond with higher equilibrium torque magnitudes. With this confidence, the model is then used to qualitatively examine the optimum load resistance to extract the maximum energy from each distinct freestream fluid velocity. Lower load resistances yield higher coefficients of power, but increase the freestream fluid velocity required to yield a torque-canceling operating point. Depending on the range of fluid velocities that a particular coaxial counter-rotating turbine is exposed to, the model can be utilized to determine the optimum constant load condition for maximum energy extraction.

4.2. Future work

The geometry of the turbine blades could be optimized for this operating regime. Future work could include testing the potential for greater power extraction if the downstream rotor is designed with the knowledge that some proportion will always be in the wake of the upstream rotor. The twist could be increased to extract power at lower freestream fluid velocities, there could be more blades, and the span could be increased or decreased to change the amount of fresh flow to the downstream depending on application. A study could be done to determine if there is an optimal twist distribution that depends on the range of freestream fluid velocity.

The scope of the experimental tests could be expanded to understand the effects of the location of the CG and CB. During testing, it was noticed that if the turbine was either slightly positively buoyant, slightly negatively buoyant, or the CB and CB were not collocated the turbine would drift to the right as it was towed across the pool. This coincides with the theoretical predictions of [10], but this effect was not experimentally quantified. In this study, the IMU was used to measure angular velocity only, but could be used to measure orientation angles. The amplitude and frequency of any oscillations could be measured. The system needs to be calibrated each time it is powered on, so a redesign would be necessary to measure this data since currently the IMU is only powered on when the watertight electronics compartment has been assembled, where the Arduino cannot be connected to a computer to run the calibration program, so a true level cannot be accomplished. Also, the system only logs data when the hall sensor has measured a magnet 100 times, so data is collected at 100 Hz but is only logged about 1 Hz depending on the tow speed. This orientation angles could give quantitative data on whether the CB and CG are truly collocated. There is also nothing currently to guarantee that the IMU is aligned with the body axes of the turbine, this should be redesigned moving forward. Since some of the turbine is flooded, the weight of the turbine out of the water cannot be used to determine the weight of the turbine when submerged, making locating the CG difficult. Also, it is suspected the closed cell foam used in the nose and tail cones and on the lid of the electronics compartment took on water as the tests progressed. The turbine would be slightly positively buoyant at the beginning of the testing campaign and would be slightly negatively buoyant by the end of the testing campaign. If these issues with locating CG and CB and IMU data collection could be resolved, then the effects of the variation in CG and CB could be quantitatively measured.

REFERENCES

[1] V. M. Lyatkher, Tidal Power : Harnessing Energy from Water Currents, John Wiley & Sons, Incorporated, 2014.

[2] A. Ipannou, A. Angus and F. Brennan, "Parametric CAPEX, OPEX, and LCOE expressions for offshore wind farms based on global deployment parameters," *Energy Sources Part B Economics Planning and Policy*, vol. 13, no. 5, pp. 281-290, 2018.

[3] M. Tomczak and J. S. Godfrey, Regional Oceanography : An Introduction, vol. I, Pergamon, 1994.

[4] M. J. Khan, G. Bhuyan, M. T. Iqbal and J. E. Quaicoe, "Hydrokinetic energy conversion systems and assessment of horizontal and vertical," *Applied Energy*, vol. 86, no. 10, pp. 1823-1835, 2009.

[5] K. Kusakana and H. J. Vermaak, "Hydrokinetic power generation for rural electricity supply: Case of South Africa," *Renewable Energy*, vol. 55, pp. 467-473, 2013.

[6] J. VanZwieten, W. McAnally, J. Ahmad, T. Davis, J. Martin, M. Bevelhimer, A. Cribbs, R. Lippert, T. Hudon and M. Trudeau, "In-Stream Hydrokinetic Power: Review and Appraisal," *Journal of Energy Engineering*, vol. 141, no. 3, pp. 04014024-1, 2015.

[7] N. D. Laws and B. P. Epps, "Hydrokinetic energy conversion: Technology, research, and outlook," *Renewable and Sustainable Energy Reviews*, vol. 57, pp. 1245-1259, 2016.

[8] M. J. Kaiser and B. Snyder, "Offshore Wind Energy Installation and Decommissioning Cost Estimation in the U.S. Outer Continental Shelf," Energy Research Group, LLC, Baton Rouge, LA, 2010.

[9] A. Pacheco, E. González-Gorbeña, T. Plomaritis and H. Gonçalves, "Lessons learned from E1 Evopod Tidal Energy Converter deployment at Ria Formosa, Portugal," in *7th International Conference on Ocean Energy*, Cherbourg, France, 2018.

[10] R. Metoyer, P. Chatterjee, K. Elfering, M. Bryant, K. Granlund and A. Mazzoleni, "Modeling, simulation, and equilibrium analysis of tethered coaxial dual-rotor ocean current turbines," *Energy Conversion and Management,* vol. 243, 2021.

[11] D. J. Olinger and Y. Wang, "Hydrokinetic energy harvesting using tethered undersea kites," *Journal of Renewable and Sustainable Energy,* vol. 7, no. 4, 2015.

[12] V. S. Neary, M. Previsic, R. A. Jepsen, M. J. Lawson, Y.-H. Yu, A. E. Copping, A. A. Fontaine, K. C. Hallett and D. K. Murray, "Methodology for Design and Economic Analysis of Marine Energy Conversion (MEC) Technologies," Sandia National Labratories, 2014.

[13] J. Clarke, G. Conner, A. Grant, C. Johnstone and S. Ordonez-Sanchez, "Analysis of a single point tensioned mooring," *IET Renewable Power Generation,* vol. 4, no. 6, pp. 473-487, 2010.

[14] B. Huang, Y. Usui, K. Takaki and T. Kanemoto, "Optimization of blade setting angles of a counter-rotating type horizontal-axis tidal turbine using response surface methodology and experimental validation," *International Journal of Energy Research,* vol. 40, no. 5, pp. 620-627, 2016.

[15] R. Saulescu, M. Neagoe and N. Cretescu, "Comparative analysis of two wind turbines with counterrotating," in *IOP Conference Series: Materials Science and Engineering*, 2020.

[16] R. W. Y. Habash, V. Groza, Y. Yang, C. Blouin and P. Guillemette, "Performance of a Contrarotating Small Wind Energy Converter," *ISRN Mechanical Engineering*, pp. 1-10, 2011.

[17] K. Appa, "Counter Rotating Wind Turbine System," Energy Innovations Small Grant Program, 2002.

[18] J. D. Booker, P. H. Mellor, R. Wrobel and D. Drury, "A compact, high efficiency contra-rotating generator suitable for wind turbines in the urban environment," *Renewable Energy*, vol. 35, no. 9, pp. 2027-2033, 2010.

[19] A. Rosenberg, S. Selvaraj and A. Sharma, "A Novel Dual-Rotor Turbine for Increased Wind Energy Capture," *Journal of Physics: Conference Series*, vol. 524, 2014.

[20] B. Huang, Y. Nakanishi and T. Kanemoto, "Numerical and experimental analysis of a counter-rotating type horizontal-axis tidal turbine," *Journal of Mechanical Science and Technology*, vol. 30, no. 2, pp. 499-505, 2016.

[21] J. Clarke, G. Conner, A. Grant, C. Johnstone and S. Ordonez-Sanchez, "Contra-rotating Marine Current Turbines: Single Point Tethered Floating System - Stability and Performance," in *8th European Wave and Tidal Energy Conference*, Uppsala, Sweeden, 2009.

[22] D. N. Khatri, P. Chatterjee, R. Metoyer, A. P. Mazzoleni, M. Bryant and K. O. Granlund, "Dual-Actuator Disc Theory for Turbines in Yaw," *AIAA Journal*, vol. 57, no. 5, pp. 2204-2208, 2019.

[23] N. J. Lee, I. C. Kim, C. G. Kim, B. S. Hyun and Y. H. Lee, "Performance study on a counter-rotating tidal current turbine by CFD and model experimentation," *Renewable Energy*, vol. 79, pp. 122-126, 2015.

[24] R. Metoyer, P. Chatterjee, K. Elfering, M. Bryant, K. Granlund and A. Mazzoleni, "Experimental analysis of dual coaxial turbines in skew," *Ocean Engineering*, vol. 215, 2020.

[25] M. Ragheb and A. M. Ragheb, Wind Turbines Theory - The Betz Equation and Optimal Rotor Tip Speed Ratio, INTECH Open Access Publisher, 2011.

[26] B. G. Newman, "Actuator-Disc Theory for Vertical-Axis Wind Turbines," *Journal of Wind Engineering and Industrial Aerodynamics*, vol. 15, no. 1-3, pp. 347-355, 1983.

[27] S. Lee, H. Kim, E. Son and S. Lee, "Effects of design parameters on aerodynamic performance of a counter-rotating wind turbine," *Renewable Energy*, vol. 42, pp. 140-144, 2012.

[28] I. Masters, J. C. Chapman, M. R. Willis and J. A. C. Orme, "A robust blade element momentum theory model for tidal stream turbines including tip and hub loss corrections," *Journal of Marine Engineering & Technology*, vol. 10, no. 1, pp. 25-35, 2011.

[29] Notre Dame, [Online]. Available: https://www3.nd.edu/~tcorke/w.WindTurbineCourse/Aerodynamics_Presentation.pdf. [Accessed 21 07 2021].

[30] R. Gasch and J. Twele, Wind power plants fundamentals, design, construction and operation, Springer, 2012.

[31] M. Ragheb and A. M. Ragheb, Fundamental and Advanced Topics in Wind Power, InTech, 2011.

[32] C. A. Lyon, A. P. Brieren, P. Giguere, A. Gopalarathnam and M. S. Selig, Summary of Low-Speed Airfoil Data, Virginia Beach, Virginia: SoarTech Publications, 1997.

[33] R. E. Wilson and P. B. S. Lissaman, Applied Aerodynamics of Wind Power Machines, 1974.

[34] A. R. Hambley, Electrical Engineering : Principles and Applications, 5 ed., Upper Saddle River, New Jersey: Pearson, 2011.

[35] [Online]. Available: https://offwegorocketry.com/userfiles/file/Nose%20Cone%20&%20Fin%20Optimization.pdf. [Accessed 21 07 2021].

[36] Electric Machinery Committee of the IEEE Power Engineering Society, "IEEE Standard Test Procedure for Polyphase Induction Motors and Generators," IEEE, New York, NY, 2004.

[37] National Instruments Corp., [Online]. Available: https://zone.ni.com/reference/en-XX/help/372062L-01/multisim/steppermotortwophase/. [Accessed 17 06 2021].

[38] [Online]. Available: https://www.amazon.com/gp/product/B071S7RMSX/ref=ppx_yo_dt_b_asin_title_o00_s00?ie=UTF8&psc=1. [Accessed 01st July 2021].